Supplementary Information for "Observation of Restored Adiabatic State Transfer in Time-Modulated Non-Hermitian Systems"

Xiaowei Wang,[1,*] Ievgen I. Arkhipov,[2,*] Quan Lin,[3] Huixia Gao,[3] Dengke Qu,[3] Lei Xiao,[3] Franco Nori,[4] and Peng Xue[3,†]

[1] *Beijing Computational Science Research Center, Beijing 100193, China*
[2] *Joint Laboratory of Optics of Palacký University and Institute of Physics of CAS, Faculty of Science, Palacký University, 17. listopadu 12, 771 46 Olomouc, Czech Republic*
[3] *School of Physics, Southeast University, Nanjing 211189, China*
[4] *Quantum Information Physics Theory Research Team, Quantum Computing Center, RIKEN, Wakoshi, Saitama, 351-0198, Japan*

CONTENTS

In this Supplementary Material, we provide details on: encircling loops on the hyperboloid manifold, the spectrum of the non-Hermitian Hamiltonian (NHH) H' and the prospective encircling trajectories around the exceptional point (EP), a proposed experimental scheme for the dynamical observation of the adiabatic state transfer, perturbation analysis, robustness analysis of evolution speed and loop parameters on restored adiabaticity, and additional supporting experimental information.

Supplementary Note 1. Encircling Loops on the Hyperboloid Manifold in the 4D Parameter Space

In the main text, we describe how the encircling loops in the (x, y) plane correspond to loops on the hyperboloid surface in the four-dimensional (4D) parameter space $[\epsilon(x, y), u(x, y), v(x, y), \kappa(x, y)]$, due to the parameterization definition in the main text. In Supplementary Fig. 1 we illustrate the actual shape of such loops on these hyperboloid surfaces in the 4D space.

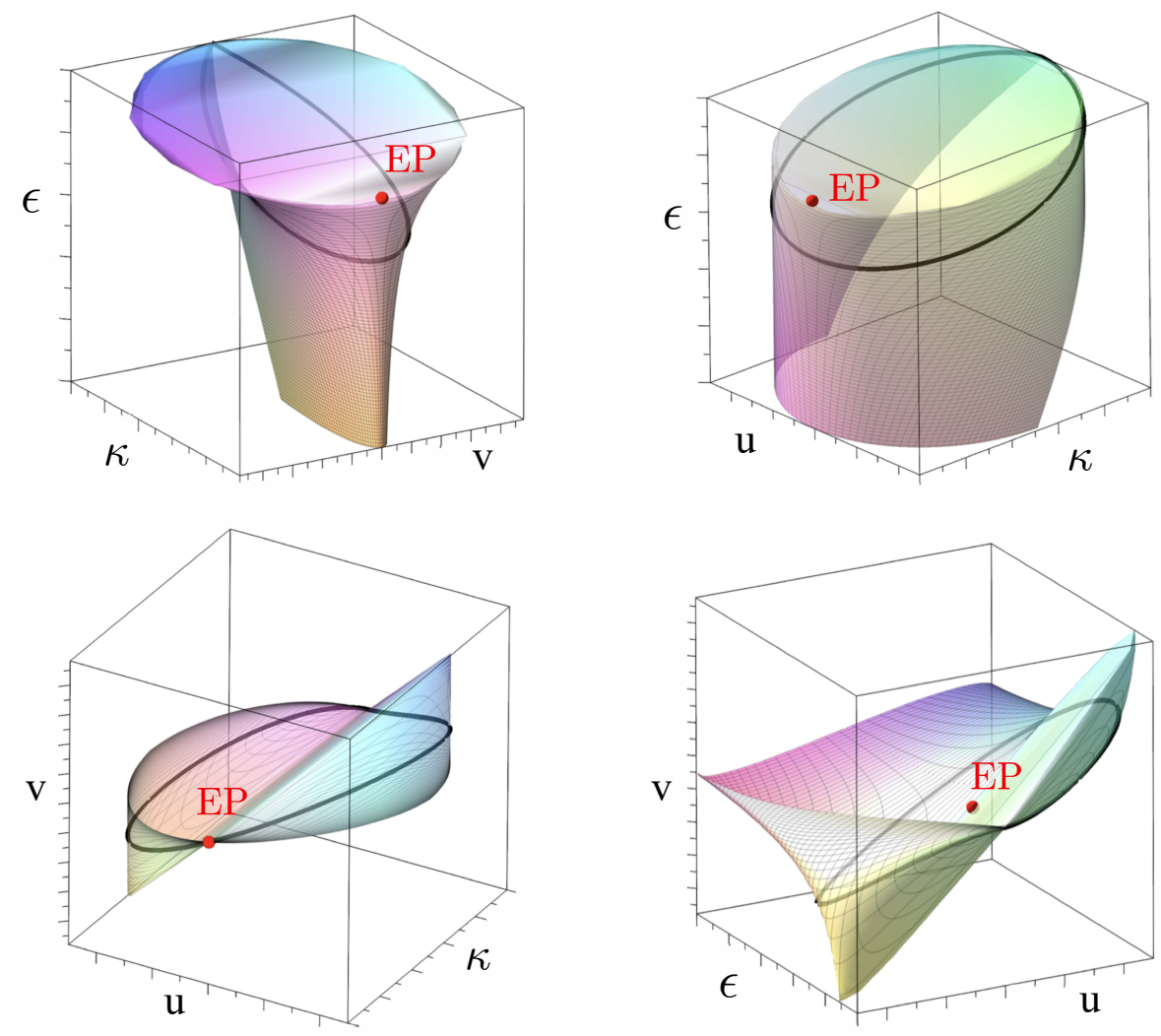

Supplementary Fig. 1. A loop (black solid curve) on the hyperboloid submanifold (shown as a 2D colored surface) encircling the exceptional point (red dot) in the 4D parameter space (ϵ, u, v, κ). The winding trajectory in 4D space is illustrated through four different 3D projections. This encircling path corresponds to a circular loop in the (x, y) plane, as defined in Eq. (3) for $r = 0.5$, and shown in Fig. 1a in the main text.

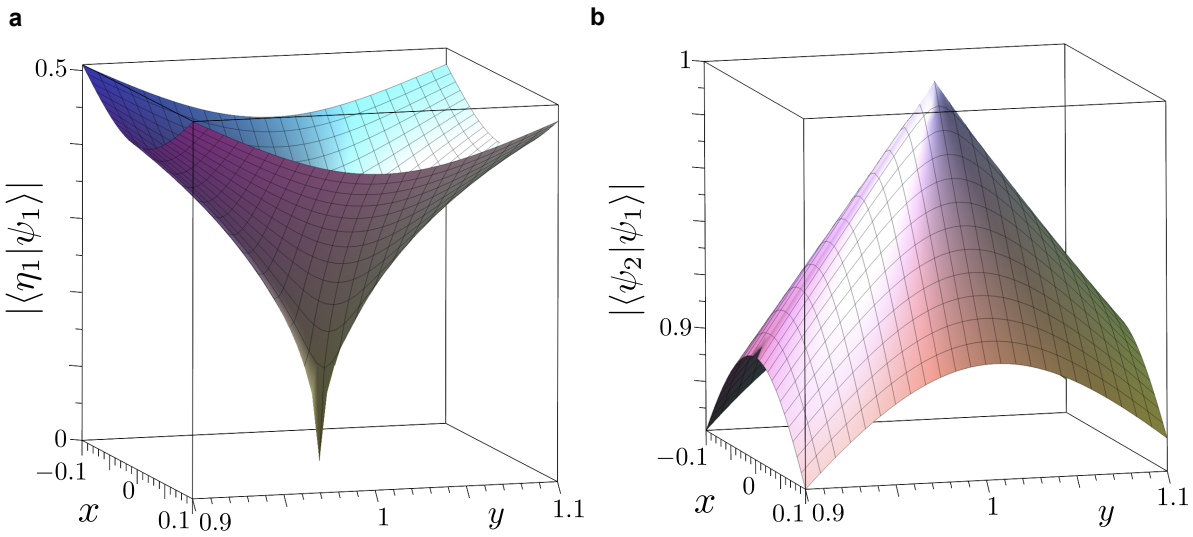

Supplementary Fig. 2. Eigenvectors overlap of the non-Hermitian Hamiltonian H_0 [Eq. (1) in the main text], demonstrating the characteristic signatures of an exceptional point (EP) in the (x, y) parameter space. **a** Biorthogonal overlap between left and right eigenvectors, which vanishes at the EP located at $(x = 0, y = 1)$, indicating self-orthogonality. **b** Overlap between the two right eigenvectors of H_0, which approaches unity at the same point, signaling the coalescence of eigenvectors at the EP.

Supplementary Note 2. Exceptional Point and Resolution of Parametrization Singularity

In the main text, we introduced a transformed non-Hermitian Hamiltonian $H_0 \to H$ obtained by mapping the system parameters onto a hyperbolic surface [Eqs. (3) and (4)]. This mapping is continuous throughout the parameter space, except at the exceptional point (EP), where the original non-Hermitian Hamiltonian H_0 becomes defective.

As a consequence, the eigenvectors of the transformed Hamiltonian H, given in Eqs. (11) and (12), exhibit an apparent divergence when approaching the EP, since $\phi \to -i\infty$ at this point. At first sight, this behavior seems inconsistent with the expected properties of an EP, where the right eigenvectors coalesce, $\langle\psi_1^{EP}|\psi_2^{EP}\rangle = 1$, and the biorthogonal norm vanishes, $\langle\eta_i^{EP}|\psi_i^{EP}\rangle = 0$ for $i = 1, 2$. This raises the question of whether the singularity in the transformed representation corresponds to a genuine EP.

To clarify this issue, it is useful to return to the original representation, where the non-Hermitian Hamiltonian H_0 [Eq. (1) in the main text] is well-defined across the entire parameter space. By tracking the behavior of its right eigenvectors $|\psi\rangle$ $(H_0|\psi\rangle = E|\psi\rangle)$ and left eigenvectors $|\eta\rangle$ $(H_0|\eta\rangle = E^*|\eta\rangle)$ as functions of the parameters (x, y), one can directly verify the defining features of an EP at these points. More specifically, we first calculate the eigenspectrum of H_0 as a function of the parameters (ϵ, u, v, κ), and then apply the hyperbolic map in Eq. (3) in the main text.

In particular, we find that the point $(x = 0, y = 1)$ indeed corresponds to an EP. At this point, the left and right eigenvectors become mutually orthogonal, and the right eigenvectors coalesce, as shown in Supplementary Fig. 2a,b, respectively. This demonstrates that the EP is well-defined in the original Hamiltonian, and that the apparent singularity arises solely from the parametrization used in the transformed Hamiltonian. Importantly, our protocol relies exclusively on encircling the EP, i.e., on trajectories that remain away from the singular point itself. Along such cyclic paths, the eigenvectors remain well-defined, ensuring the consistency of the description.

Supplementary Note 3. Dynamical Mapping via Discretized Unitary Decomposition

To elucidate the correspondence between the target physical model and our experimental setup in Fig. 1(b) of the main text, we provide a schematic representation of the simulation protocol in Supplementary Fig. 3. This diagram illustrates how the continuous dynamics of the target system is mapped onto the controllable quantum simulator through state preparation, a single-pass of light through the optical setup, and final measurement.

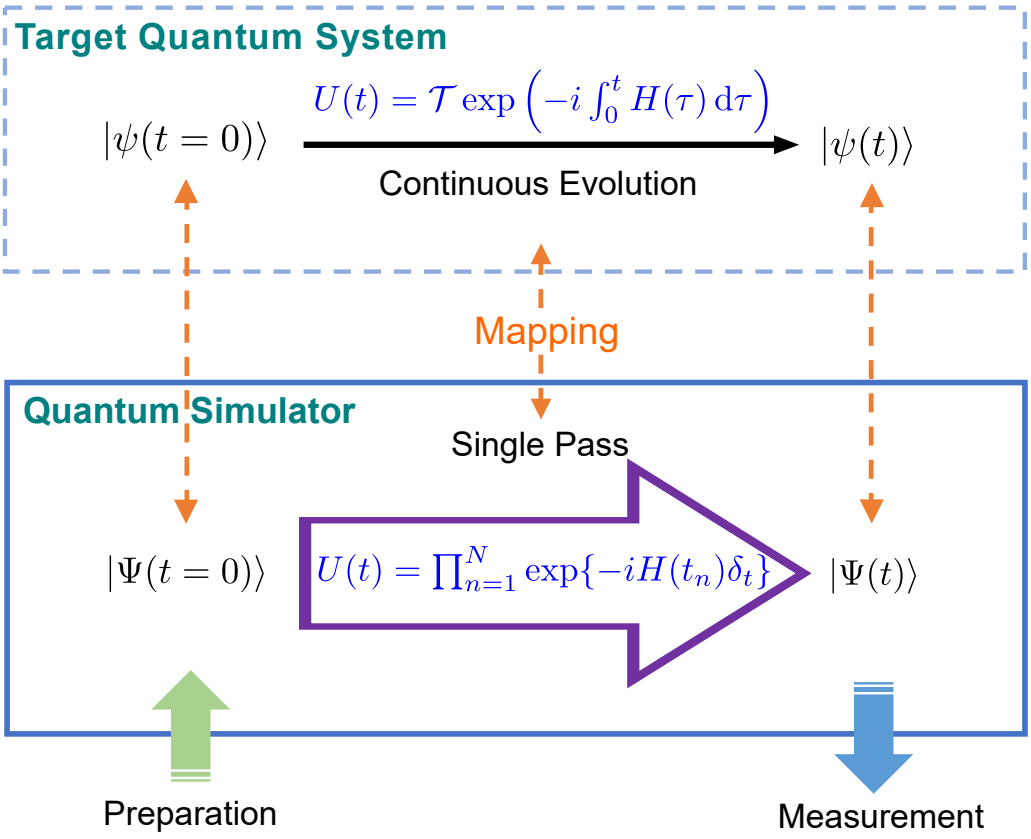

Supplementary Fig. 3. Schematic illustration comparing a target quantum system with its corresponding quantum simulator. The target system (top) evolves from an initial state $|\psi(t=0)\rangle$ to a final state $|\psi(t)\rangle$ under the governing Hamiltonian $H(t)$. The simulator (bottom) replicates this dynamics through a controllable process. Specifically, the simulator is initialized in state $|\Psi(t=0)\rangle$ and driven through a single pass of the discretized unitary evolution $U(t) = \prod_{n=1}^{N}\exp\{-iH(t_n)\delta_t\}$ to reach $|\Psi(t)\rangle$. The vertical dashed orange arrows indicate the mapping correspondence between the target and simulated states. The upward green arrow and downward blue arrow denote the state preparation and measurement phases, respectively. The detailed experimental implementation can be shown in Fig. 1(b) of the main text.

Supplementary Note 4. The Form of States in the Polarization Representation

In optics, polarized light can be described by the Jones calculus developed by R. C. Jones in 1941 [1]. Polarized light is represented by Jones vectors, and linear optical elements are represented by Jones matrices. For an arbitrary polarized light, it can be represented by two orthogonal linear polarization components. Here, we generally select horizontal and vertical polarizations, which can be well separated using a polarizing beam splitter. Using the Jones matrix notation, the complex amplitudes of the two orthogonal components of the polarized light are:

$$\vec{J}(t) = \begin{bmatrix}\hat{E}_X \\ \hat{E}_Y\end{bmatrix} = \begin{bmatrix}E_X e^{i(\omega_0 t - k_0 Z + \delta_X)} \\ E_Y e^{i(\omega_0 t - k_0 Z + \delta_Y)}\end{bmatrix} = \exp\left(i(\omega_0 t - k_0 Z + \delta_X)\right)\begin{bmatrix}E_X \\ E_Y e^{i\delta_D}\end{bmatrix}, \tag{S1}$$

where $\delta_D = \delta_Y - \delta_X$ represents the phase difference between the two components, ω_0 and k_0 denote the angular frequency and the wavenumber, E_X and E_Y are their amplitudes. By omitting the identical factors, the general expression of the Jones vector after normalization can be written as:

$$\vec{J} = \frac{1}{\sqrt{E_X^2 + E_Y^2}}\begin{pmatrix}E_X \\ E_Y e^{i\delta_D}\end{pmatrix}. \tag{S2}$$

Based on the above discussion, we can also use the polarization ellipse and the Poincaré sphere with Stokes parameters to more intuitively describe the polarization of light [2].

Supplementary Note 5. Fidelity Between Evolving and Initial States

In Fig. 2 in the main text, we present experimental plots of the instantaneous eigenstate population of the NHH in Eq. (2). Here, in Supplementary Fig. 4, we provide complementary plots for the fidelity between the evolving and static initial states instead, thus further confirming the observed adiabatic and *continuous* symmetric state switching mechanism.

We notice that there is a lower limit for the fidelity in Supplementary Fig. 4. This theoretical lower bound is determined by the state overlap of the instantaneous eigenstates $|\psi_1(0)\rangle$ and $|\psi_2(0)\rangle$ at the initial time. This result is attributed to our intentional protocol design, which aims to maximize the energy gap between the two levels $E_{1,2}$ at time $t = 0$; thus ensuring that the initial states have an overlap as minimal as possible, and which equals $\sim 4/9$.

Compared with Fig. 2 in the main text, we note that the fidelity is significantly more sensitive to noise and experimental imperfections than the population metric P utilized in the main text.

The relative eigenstate population P, given in Eq. (9) in the main text, is calculated within the biorthogonal basis. In non-Hermitian systems, the right eigenstates $\{|\psi_m\rangle\}$ are not mutually orthogonal, but they form a biorthogonal basis with the left eigenstates $\{|\eta_n\rangle\}$, satisfying the condition $\langle\eta_n|\psi_m\rangle = \delta_{mn}$. To obtain the relative population P experimentally, we project the measured state $|\psi_{\rm exp}\rangle$ onto the left eigenvectors of the Hamiltonian (i.e., calculating overlaps like $\langle\eta_n|\psi_{\rm exp}\rangle$). This biorthogonal projection effectively "filters out" the contribution from the unwanted mode due to the orthogonality condition $\langle\eta_n|\psi_m\rangle = 0$ $(m \neq n)$. Consequently, the population metric P is inherently robust and less sensitive to small imperfections in the evolved state, leading to better agreement between theory and experimental data.

In contrast, the state fidelity, is defined as the direct overlap magnitude $F = |\langle\psi_k|\psi_{\rm exp}\rangle|^2$ between the initial and experimentally evolving right states. Consequently, it becomes highly sensitive to all forms of experimental noise, including global phase fluctuations and intensity drifts. The scatter observed in Supplementary Fig. 4 reflects this hypersensitivity to experimental noise, rather than a fundamental deviation from the theoretical predictions.

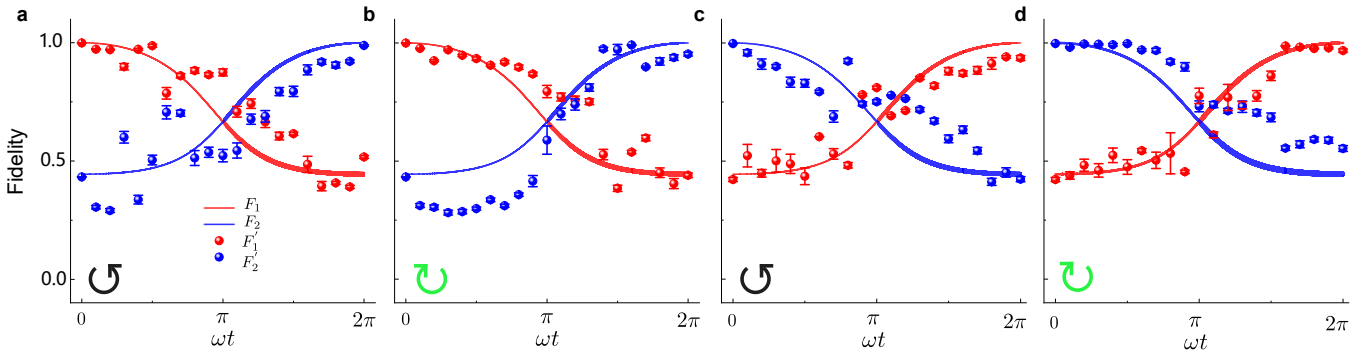

Supplementary Fig. 4. Fidelity between the evolving and initial states. This is complementary to Fig. 2 of the main text. **a-b**: The initial state is chosen as $|\psi_1\rangle$ on the E_1 energy surface. **c-d**: The initial state is chosen as $|\psi_2\rangle$ on the E_2 energy surface. Fidelity $F_k = |\langle\psi_k(t)|\Psi_{\rm th}(t)\rangle|^2$ $(k = 1, 2)$ quantifies the overlap between the theoretical time-evolving right eigenstate $|\Psi_{\rm th}(t)\rangle$ and instantaneous right eigenvector $|\psi_k(t)\rangle$ of the NHH. Similarly, $F_k' = |\langle\psi_k(t)|\Psi_{\rm exp}(t)\rangle|^2$ $(k = 1, 2)$ denotes the fidelity between the evolving experimental state $|\Psi_{\rm exp}(t)\rangle$ and instantaneous right eigenvector $|\psi_k(t)\rangle$ of the NHH while encircling the EP. The state is normalized at each moment, ensuring that the fidelity always lies between 0 and 1. The discrepancy between experiment and theory mainly stems from the uncertainty of the instantaneous eigenstates and unavoidable noise during the experiment, as well as the nonlinear quantitative relationship between the fidelity and system states. Other system parameters are identical to Fig. 2.

Supplementary Note 6. The Spectrum of the NHH H' and the Encircling Trajectories Around the EP

As shown in Supplementary Fig. 5, we plot the energy spectrum of the NHH H' of the main text. Importantly, the spectrum of H', compared to H, exhibits the imaginary part, which plays the key role in inducing the NATs. To investigate the state transfer process under such circumstances, we construct the trajectory of the state evolution over the Riemann surface of the non-Hermitian Hamiltonian as follows:

$$\bar{E}(t) = \frac{\sum_{i=\pm} E_i(t)|\langle\eta_i(t)|\psi(t)\rangle|^2}{\sum_{i=\pm}|\langle\eta_i(t)|\psi(t)\rangle|^2}, \tag{S3}$$

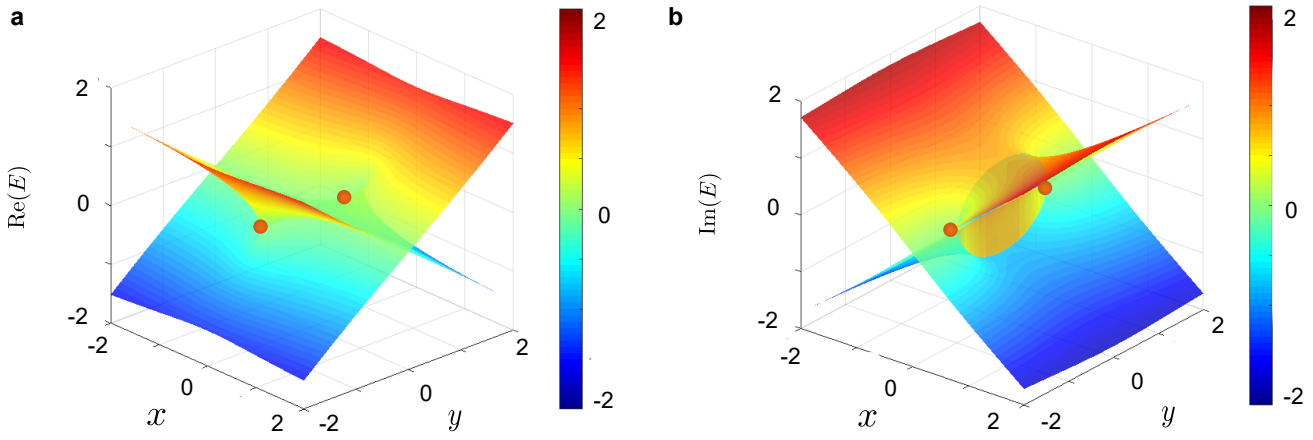

Supplementary Fig. 5. The eigenenergy spectrum of the NHH H' in Eq. (4). **a** Real energy spectrum and **b** imaginary energy spectrum. The small orange spheres represent the EP points.

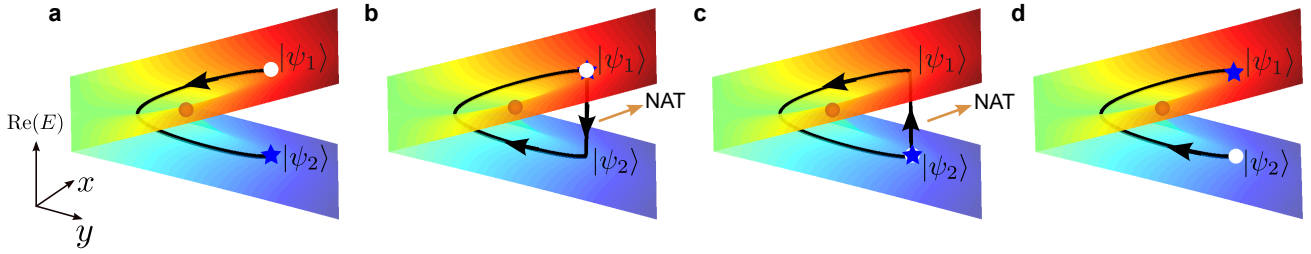

Supplementary Fig. 6. Prospective encircling trajectories in the parameter space for the dynamics of two states with starting points on different sheets. The arrow indicates the encircling direction around the EP. **a**, **c** Counter-clockwise direction. **b**,**d**: Clockwise direction. The starting positions are shown as white circles, and the evolved endpoints are represented by blue stars. **a-b** The initial state is chosen as $|\psi_1\rangle$. **c-d** The initial state is chosen as $|\psi_2\rangle$. **b-c** The starting point and the ending point coincide, indicating that after one cycle of evolution, it returns to its original state. In this case, non-adiabatic transitions (NATs) occur.

where $|\psi(t)\rangle$ is the evolving state governed by the NHH and $|\eta_i(t)\rangle$ is the left eigenvector.

To demonstrate the non-adiabatic nature of dynamically encircling an EP, we show trajectories on real energy surfaces with different encircling directions, starting on both of the Riemann sheets involved (shown as red and blue surfaces), as shown in Supplementary Fig. 6. We observe that the state that survives at the end of a loop is independent of the initial state and depends solely on the direction of the loop. Counterclockwise looping always results in a state on the lower-energy plane, while clockwise looping always results in a state on the upper-energy plane, exhibiting chiral characteristics. It is not difficult to find that this chiral mode behavior is caused by non-adiabatic transitions, as shown in Supplementary Figs. 6b,c. This result is consistent with the results in Fig. 3 of the main text.

Supplementary Note 7. A Proposed Experimental Scheme for the Continuous Observation of the Adiabatic State Transfer

Recently, increasingly refined time-control techniques in photonic simulators have been explored [5], offering new insights into the characterization of the full dynamics of physical systems. Then, we further refine our experimental setup by extending it into a fiber-loop structure, thereby additionally proposing an experimental scheme that allows to monitor the adiabatic time evolution of light in a continuous round-trip direct-detection system. By applying time-controlled intensity and phase modulations along with polarization coupling, each round trip in the loop effectively corresponds to a distinct point in the parameter space. Extensive numerical simulations of this non-Hermitian setup allow us to provide a more comprehensive depiction of adiabatic state transitions in such platforms. Further details

are provided below.

To realize the full adiabatic evolution, we can decompose the total time-evolution operator $U(t)$ into a product of small-segment unitary operations. Each segment is approximated as $U_n = e^{-iH(t_n)\delta_t}$, where $n = 1, 2, \ldots, N$, and δ_t is the time interval of each segment. We first perform a general decomposition of U as:

$$U_n = R_n^1 L_n R_n^2, \tag{S4}$$

where $n = 1, 2, \ldots, N$, R_n^1 and R_n^2 are 2×2 unitary operators, and L_n is a 2×2 diagonal operator. The following describes how to implement it: As illustrated in Supplementary Fig. 7, the initial eigenstate can be encoded in the polarization state of the light pulse $|\Psi(0)\rangle = [a_0, b_0]^T$, and then coupled into the fiber loop via the beam splitter (BS). Next, the polarization controller (PC1) can realize R_n^1; this is because the polarization controller can be equivalently represented as a sandwiched combination of two quarter-wave plates and one half-wave plate (Q-H-Q), which can achieve the required 2×2 unitary transformation.

According to the Jones matrix form of the half-wave plate in Eq. (9) and the Jones matrix form of the quarter-wave plate in Eq. (10), the optical pulse after undergoing the operation of PC1 can be universally expressed as

$$\begin{pmatrix} a_n^{(1)} \\ b_n^{(1)} \end{pmatrix} = R_n^1(\varsigma_2, \varphi_1, \varsigma_1) \begin{pmatrix} a_n \\ b_n \end{pmatrix}, \tag{S5}$$

where $R_n^1(\varsigma_2, \varphi_1, \varsigma_1) = U_q(\varsigma_2) U_h(\varphi_1) U_q(\varsigma_1)$. Then we use a polarization beam splitter (PBS) to guide the horizontal and vertical field components to two separate branches, where they are independent but simultaneously undergo different gain or loss modulation, thus enabling us to achieve a diagonal 2×2 matrix L_n. These respective modulations are realized by introducing loop-dependent gain and phase modulations to these polarization components,

$$\begin{pmatrix} a_n^{(2)} \\ b_n^{(2)} \end{pmatrix} = L_n \begin{pmatrix} a_n^{(1)} \\ b_n^{(1)} \end{pmatrix} = \begin{pmatrix} g_n & 0 \\ 0 & p_n \end{pmatrix} \begin{pmatrix} a_n^{(1)} \\ b_n^{(1)} \end{pmatrix}, \tag{S6}$$

Then, the two components are recombined using a polarization beam combiner (PBC). Afterwards, another polarization controller (PC2) realizes the unitary operator $R_n^2(\varsigma_4, \varphi_2, \varsigma_3)$ in a similar way. The full transformation in a single round trip is thus given by

$$\begin{pmatrix} a_{n+1} \\ b_{n+1} \end{pmatrix} = U_n \begin{pmatrix} a_n \\ b_n \end{pmatrix} = R_n^2(\varsigma_4, \varphi_2, \varsigma_3) \begin{pmatrix} g_n & 0 \\ 0 & p_n \end{pmatrix} R_n^1(\varsigma_2, \varphi_1, \varsigma_1) \begin{pmatrix} a_n \\ b_n \end{pmatrix}. \tag{S7}$$

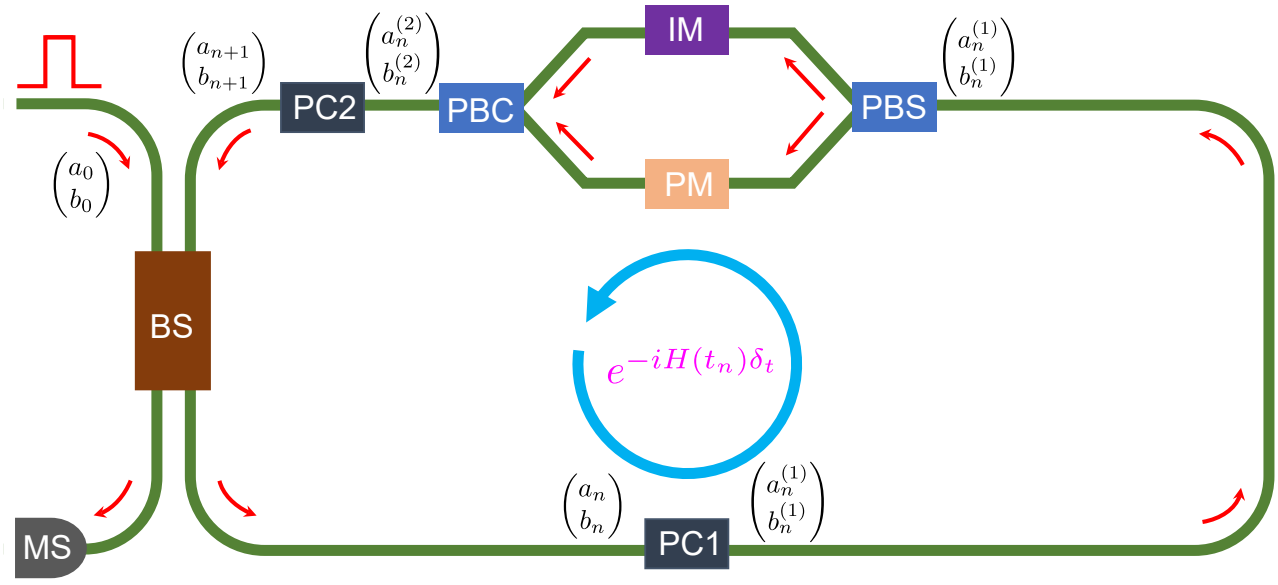

Supplementary Fig. 7. Schematic illustration of the fiber-loop arrangement for the full observation of adiabatic state evolution around the EP. BS: Beam splitter, PC: Polarization controller, PBS: Polarization beam splitter, IM: Intensity modulator, PM: Phase modulator, PBC: Polarization beam combiner and MS: Measurement system. A single loop realizes the time evolution operator $e^{-iH(t_n)\delta_t}$ for a small segment, and multiple round trips collectively implement the full evolution $U(t)$.

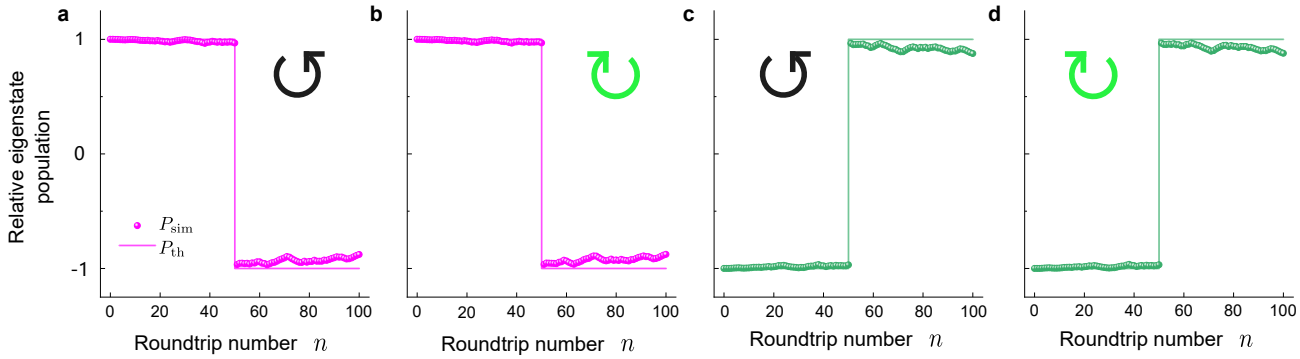

Supplementary Fig. 8. Numerical simulations of the proposed protocol for continuous observation of adiabatic state transfer. **a-b** The initial state is chosen as $|\psi_1\rangle$. **c-d** The initial state is chosen as $|\psi_2\rangle$. The relative eigenstate population $P_{\rm sim}(t)$ is obtained based on our proposed scheme with a dynamic encirclement of the EP. Solid curves denote theoretical prediction results. We set the total roundtrip number $N = 100$, meaning the full encircling period $T = 2\pi/\omega$ is discretized into 100 segments. Each roundtrip corresponds to a time step $\delta_t = T/N$. We note an abrupt change in the instantaneous eigenstates at $t = T/2$ in Fig. 2 of the main text, which precisely corresponds to the moment the evolution trajectory adiabatically transfers from one energy surface to another. Here, the same behavior is observed: the state transfer always occurs earliest at $t = T/2$, which corresponds to the roundtrip number $N/2 = 50$. The discrepancy between the simulation and theoretical results stems from the accumulation of errors. Other parameters are the same as those used in Fig. 2.

Ultimately, by sequentially modulating the optical pulse over N round trips in the fiber loop, we effectively realize the time-evolution operation $U(t)$.

We emphasize that the scheme presented here differs from our experimental setup in Fig. 1b of the main text. In Fig. 1b of the main text, each experiment implements a complete time-evolution operator $U(t)$, corresponding to one of 21 discrete time points. The design of each $U(t)$ is constructed from the product of multiple segments, and only the final state is measured per run. It also differs from standard spatially non-uniformly coupled waveguide systems, where information about the optical state is only available at the input and output ports. In contrast, the proposed scheme enables a full simulation of the adiabatic evolution by directly implementing each small segment $U_n = e^{-iH(t_n)\delta_t}$ in a sequential manner. In this scheme as illustrated in Supplementary Fig. 7, at the end of each round trip, half of the pulses couple out of the optical fiber loop for monitoring purposes, while the remaining pulses remain in the loop to repeat the process until the required number of pulse cycles is reached. Each complete loop can realize the time evolution $e^{-iH(t_n)\delta_t}$ of a small segment, and multiple round trips can implement $U(t)$, i.e., each round trip in the fiber loop realizes a single segment, and the total evolution is reconstructed through repeated cycling. This cumulative approach allows us to faithfully capture the continuous evolution dynamics, including finer features of the adiabatic process. However, this implementation requires significantly greater experimental complexity. Precise temporal control is essential for both phase and amplitude modulators triggered by a time-related arbitrary waveform generator, as well as polarization management. As a result, high-speed, high-precision instrumentation is necessary to ensure the fidelity of the evolution.

We additionally conduct numerical simulations of the proposed single-fiber experimental protocol. For that, we perform 100 iterations of the operation with roundtrip number N set to 100. As shown in Supplementary Fig. 8, the simulation results clearly demonstrate the adiabatic state transfer, and we observe good agreement with the theoretical results, which significantly improves the simulation of adiabatic state evolution. This behavior can be well understood: a higher roundtrip count corresponds to a smaller time interval, thereby enhancing simulation accuracy and better approximating the slow time-dependent adiabatic evolution process.

As shown in the Supplementary Fig. 9, based on the fiber loop simulator we previously discussed, we also numerically simulate the state transfer dynamics for a static initial eigenstate, and find that mutual transfer between the two initial states also occurs, regardless of the direction of encirclement around the EP.

Supplementary Note 8. Evolution of the Polarization Components in the Measured States

In this section, we plot the evolution of the Stokes vector components (S_1, S_2, S_3) of the experimentally measured states, providing a complete characterization of the state transfer evolution under different encirclements around the EP.

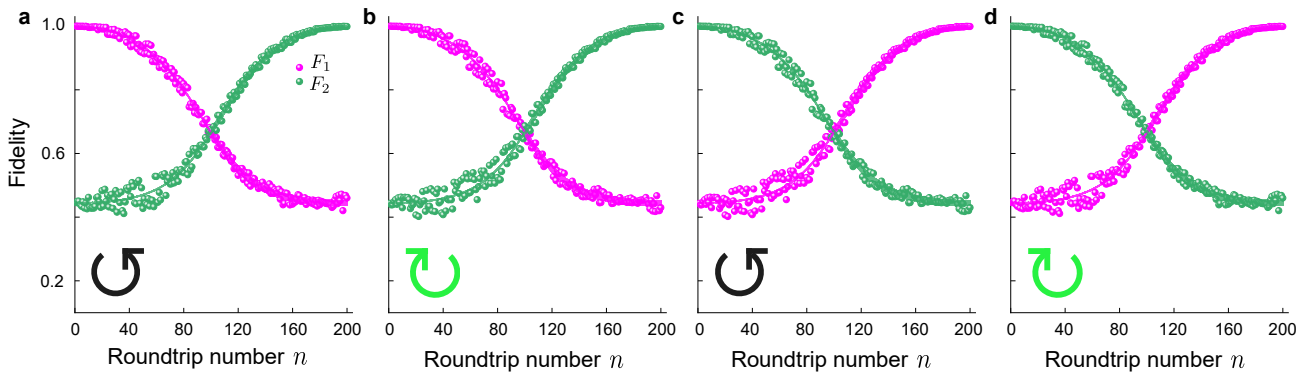

Supplementary Fig. 9. Numerical simulations of the adiabatic state transfer related to the initial right eigenvector while dynamically encircling around an EP. We set the total roundtrip number $N = 200$. **a-b** The initial state is chosen as $|\psi_1\rangle$. **c-d** The initial state is chosen as $|\psi_2\rangle$. $F_k = |\langle\psi_k(t=0)|\Psi_{\rm sim}(t)\rangle|^2$ $(k = 1, 2)$ is the fidelity between the simulated time-evolving right eigenstate $|\Psi_{\rm sim}(t)\rangle$ based on the scheme and static right eigenvector, i.e., the initial state of the system $|\psi_k(t=0)\rangle$. Solid curves are obtained from fidelity between the theoretical time-evolving right eigenstate $|\Psi_{\rm th}(t)\rangle$ and the initial state of the system.

Supplementary Figure 10a illustrates the adiabatic state transfer. In this regime, the evolution is largely symmetric with respect to the encirclement direction, demonstrating the robustness of the adiabatic mapping. The S_1 component, in particular, demonstrates a robust adiabatic-symmetric transfer regardless of the encircling direction, which is closely mirrored by the dynamics observed in Fig. 2 and Supplementary Fig. 4. In contrast, Supplementary Fig. 10b depicts the chiral state transfer dynamics. Here, we observe a distinct breaking of the winding symmetry in the state transfer. Specifically, the final configuration of the component S_1 depends fundamentally on the chirality (direction) of the encirclement around the EP, which is independent of the initial state. This behavior is in good agreement with the results presented in Fig. 3.

Supplementary Note 9. Perturbation Analysis of the Observed Adiabatic Mode Switching

In this section, we analyze the impact of perturbations of the NHH on adiabatic state transfer during the dynamic encirclement of an EP. The system's state evolution can change drastically depending on the nature of the Hamiltonian perturbations, primarily because such perturbations can render the NHH eigenvalues complex-valued. This may induce NATs in the system dynamics.

We note that a simple uniform imaginary shift of the NHH eigenvalues, i.e., $H''(t) = H(t) + i\Delta I$, where I is the identity matrix and $\Delta \in \mathbb{R}$, does not affect adiabatic state transfer. For a NAT to occur, the imaginary parts of the two eigenvalues must, in general, be different. This difference ensures that during the dynamic EP encirclement, the system may undergo a non-adiabatic transition, favoring the eigenstate belonging to the energy manifold with the larger imaginary part.

Consider instead perturbing the NHH in Eq. (3) as

$$H''(t) = H(t) + \begin{pmatrix} \Delta & 0 \\ 0 & 0 \end{pmatrix}, \tag{S8}$$

which yields the eigenenergies $E''_{1,2} = \frac{1}{2}\left(\Delta \mp \sqrt{\Delta^2 + 4\alpha^2 + 4\alpha\Delta\cos\theta}\right)$. Thus, the difference between the imaginary parts of the eigenvalues, $\mathrm{Im}(E''_2 - E''_1)$, increases with $|\Delta|$. This increase can eventually lead to the emergence of NATs and, specifically, to chiral mode behavior.

We illustrate the effect of this perturbation on the state-transfer fidelity in Supplementary Figs. 11-12 for different values of Δ. The relative eigenstate population is obtained identically to that shown in Fig. 2 of the main text.

As shown in Supplementary Fig. 11, adiabatic state transfer persists for very small ($\Delta \leq 0.03$). However, the evolving states begin to acquire an exponential factor due to the loss of pseudo-Hermiticity in the perturbed NHH H'', whose eigenvalues become complex. This exponential factor results either in damping or amplification of the evolving state. However, at larger perturbation strengths ($\delta \geq 0.05$), adiabaticity breaks down, leading to NATs and consequently to chiral mode behavior, as demonstrated in Supplementary Fig. 12.

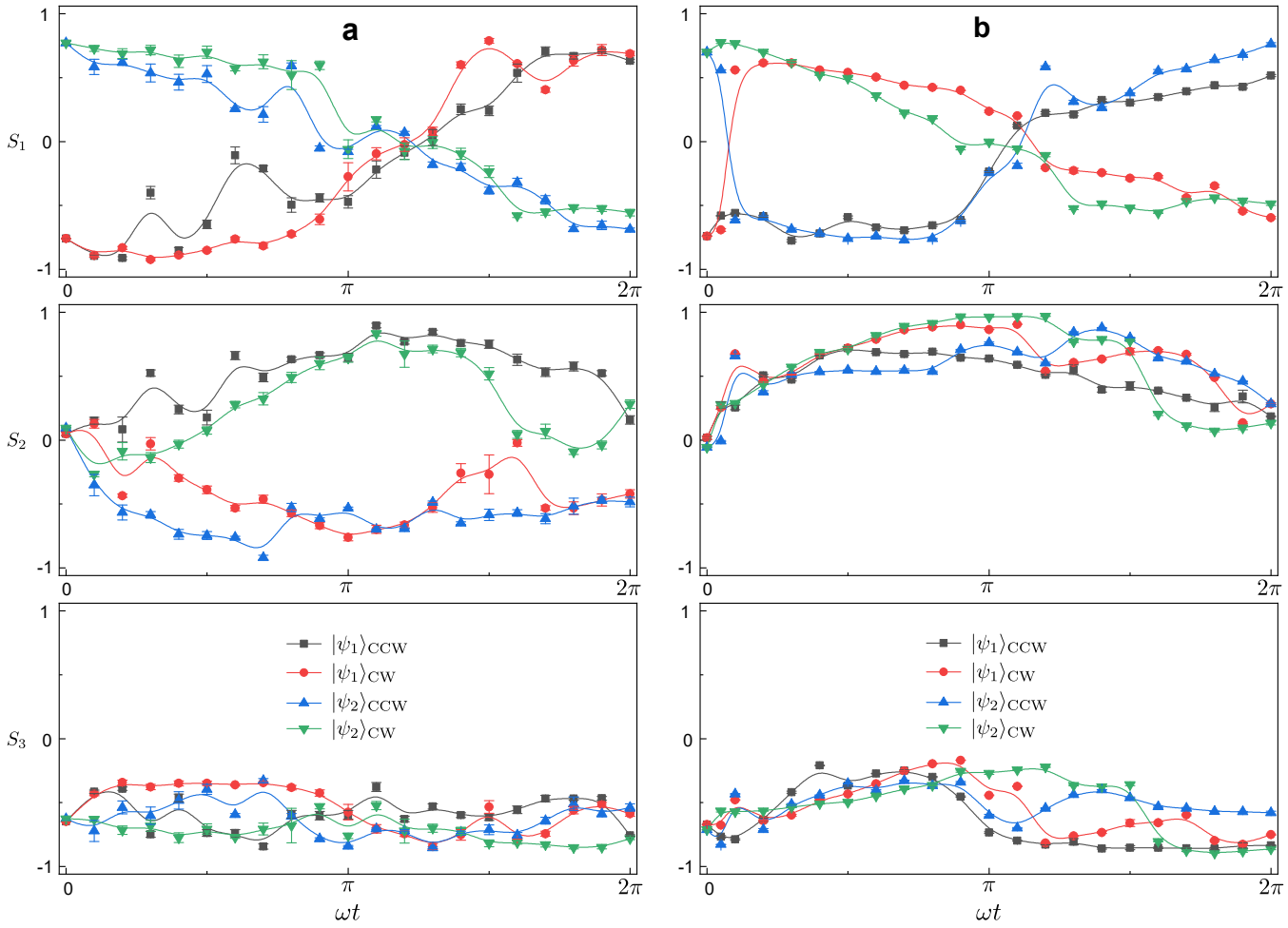

Supplementary Fig. 10. Evolution of the Stokes vector components components S_1, S_2, and S_3 during (**a**) adiabatic state transfer and (**b**) chiral state transfer. Data points represent experimental measurements for two distinct initial states, $|\psi_1\rangle$ (black and red) and $|\psi_2\rangle$ (blue and green), and the solid curves are obtained by smoothly fitting the experimental data. The markers labeled "CW" and "CCW" indicate clockwise and counter-clockwise encirclements around the EP, respectively. The trajectories of evolution illustrate the state transfer process within the adiabatic/non-adiabatic framework, where the final state distributions reflect the geometric properties of the system. The deviations are dominated by experimental imperfections in implementing the non-unitary evolution operator and measurement uncertainties. Other parameters are the same as those used in Fig. 2.

Supplementary Note 10. Impact of Evolution Speed and Loop Parameters on Restored Adiabaticity and Robustness Analysis

In this section, we present additional numerical results supporting our experimental observations of adiabatic state dynamics. By analyzing the interplay between the discretization step N, the evolution speed ω, and the loop parameters, we numerically show that the observed adiabatic state transfer is robust and reliably reproduced across a wide range of conditions.

Firstly, we plot the new numerically simulated fidelity in Supplementary Fig. 13, which complement the experimental data shown in Fig. S3. These simulations present the fidelity of the evolving state for different values of the winding period T. The newly added plots demonstrate that, in the adiabatic (slow-driving) limit $T \to \infty$, the state evolution remains continuous and the state-switching protocol is robust. By contrast, for sufficiently short winding periods, diabatic effects emerge, leading to deviations from the ideal evolution along the eigenenergy manifolds and a breakdown of the state-switching protocol.

Next, we examine the role of the discretization step N used to obtain the experimentally implemented non-unitary operator $U(t)$ in the simulated dynamics. Setting the evolution speed to $\omega = \pi/50000$, we computed the relative eigenstate population $P(t)$ as a function of N, ranging from 10 to 10^4, as shown in Supplementary Fig. 14. The

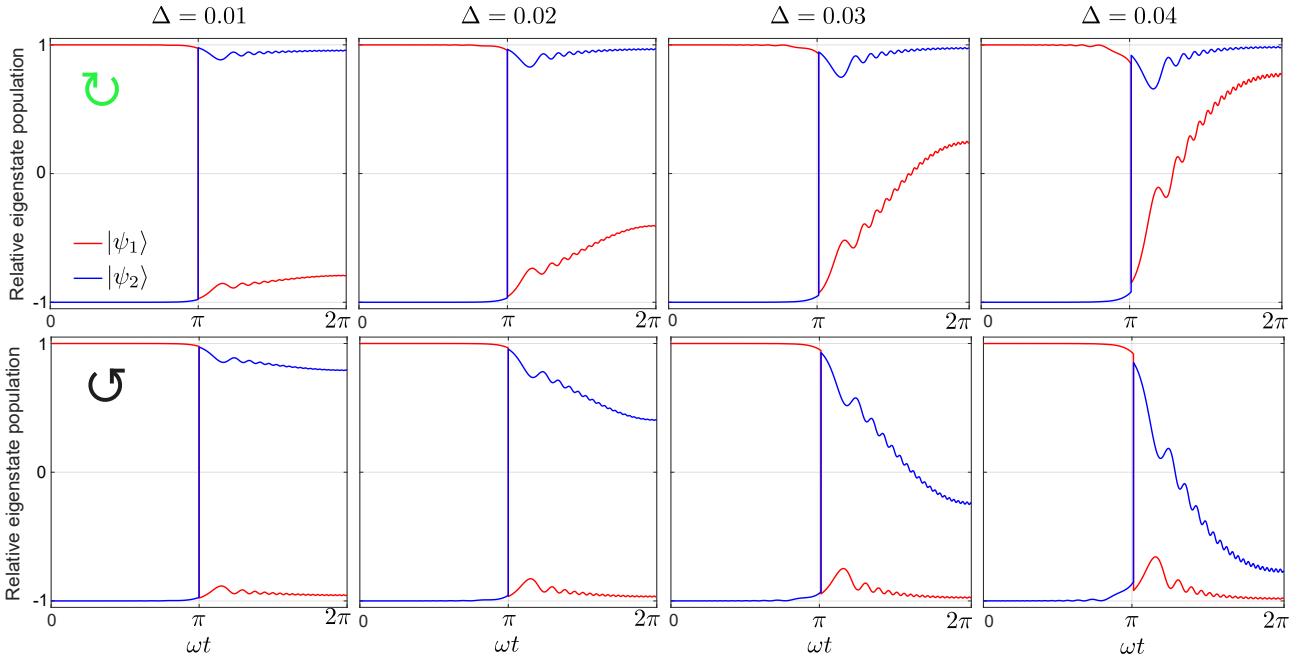

Supplementary Fig. 11. Relative eigenstate population $P(t)$ for clockwise (top row) and counter-clockwise (bottom row) parameter encirclements for different Δ while encircling the EP for Eq. (S8) at $\omega = \pi/100$. The red curves represent the evolution starting from the initial state $|\psi_1\rangle$, while the blue curves denote the evolution from $|\psi_2\rangle$. Other descriptions are the same as those used in Fig. 2.

results show that $P(t)$ rapidly converges to unity as N increases, with fluctuations becoming negligible for $N \gtrsim 1000$. For the experimental choice of $N = 50,000$ (used in the main text), the population is effectively constant, reflecting highly stable adiabatic state transfer. The consistent behavior observed in both the top and bottom rows further highlights the inherent symmetry of the protocol. These findings confirm that, unlike chiral EP encirclement, the restored adiabaticity is optimized in the adiabatic limit ($\omega \to 0$) and remains robust with respect to the encirclement direction. In contrast, for small N, the adiabatic behavior deteriorates significantly and may even vanish entirely.

To further explore the role of the evolution speed ω (with total evolution time $T = 2\pi/\omega$) on the adiabatic behavior, we numerically calculate $P(t)$ for various ω at fixed values of N, as shown in Supplementary Figs. **15**–**18**. The results demonstrate that the evolution speed critically influences adiabaticity: slower evolution (smaller ω) promotes more pronounced adiabatic behavior, whereas even with large N, adiabaticity is suppressed if ω is too large. As N increases ($N > 100$) and ω decreases ($\omega < \pi/100$), the system rapidly converges to a highly stable and symmetric adiabatic transfer, independent of the winding direction, confirming the robustness of the protocol in the high-N and low-ω limits.

As shown in Supplementary Figs. **19**-**20**, we also numerically evaluate the robustness of the scheme by varying the loop parameters, which control the "size" (the radius r and center) of the trajectory in parameter space. In Supplementary Fig. **19**, the center of the trajectory is located at the EP, $(x, y)_{\rm EP} = (0, 1)$. One can see that, regardless of the value of the radius r, the state evolution exhibits adiabatic characteristics. While the center of the trajectory is located at $(x, y) = (0, 2)$ in Supplementary Fig. **20**, only when $r > 1$ and the trajectory precisely encircles the EP, does adiabatic state exchange occur. These results demonstrate that as long as the trajectory remains on the real-spectrum hyperboloid manifold and encircles the EP, the symmetric adiabatic transfer is preserved. This highlights the topological protection inherent in our scheme.

We thus confirm that the adiabatic state transfer is observed for both clockwise and counter-clockwise encirclement directions, highlighting the intrinsic symmetry of the protocol. Taken together, these numerical results provide clear support for the conclusion that the experimentally observed "restored adiabaticity" reflects a robust and reproducible physical phenomenon.

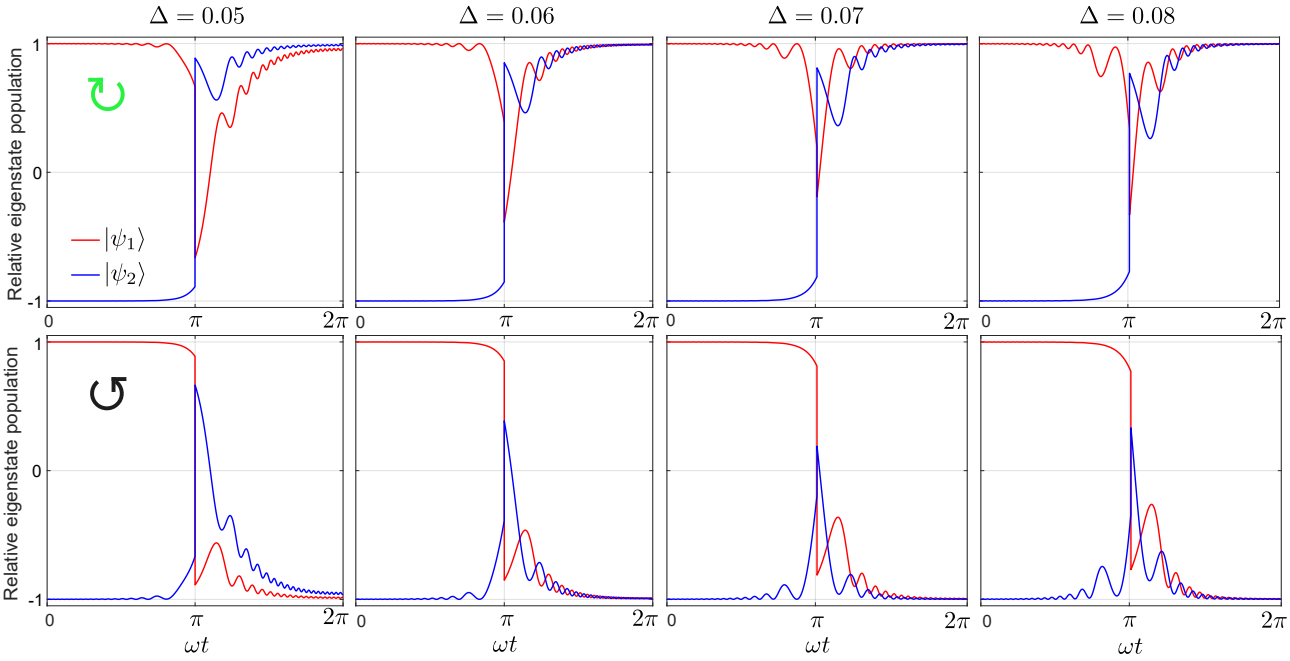

Supplementary Fig. 12. Relative eigenstate population $P(t)$ for clockwise (top row) and counter-clockwise (bottom row) parameter encirclements for different Δ while encircling the EP for Eq. (S8). Other descriptions are the same as those used in Supplementary Fig. **11**.

* These authors contributed equally to this work.
† gnep.eux@gmail.com

[1] R. C. Jones, A new calculus for the treatment of optical systems I. description and discussion of the calculus, J. Opt. Soc. Am. **31**, 488–493 (1941).
[2] E. Hecht, Optics (Addison Wesley, New York, 2016).
[3] W. Qin, C. Wang, Y. Cao, and G. L. Long, Multiphoton quantum communication in quantum networks, Phys. Rev. A **89**, 062314 (2014).
[4] X. Cheng, K. C. Chang, Z. Xie, M. C. Sarihan, Y. S. Lee, Y. Li, X. A. Xu, A. K. Vinod, S. Kocaman, M. Yu, P. G. Q. Lo, D. L. Kwong, J. H. Shapiro, F. N. C. Wong, and C. W. Wong, A chip-scale polarization-spatial-momentum quantum swap gate in silicon nanophotonics, Nat. Photonics **17**, 656–665 (2023).
[5] H. Nasari, G. Lopez-Galmiche, H. E. Lopez-Aviles, A. Schumer, A. U. Hassan, Q. Zhong, S. Rotter, P. LiKamWa, D. N. Christodoulides, and M. Khavjavikhan, Observation of chiral state transfer without encircling an exceptional point, Nature **605**, 256–261 (2022).
[6] W. Qin, C. Wang, Y. Cao, and G. L. Long, Multiphoton quantum communication in quantum networks, Phys. Rev. A **89**, 062314 (2014).
[7] J. Feilhauer, A. Schumer, J. Doppler, A. A. Mailybaev, J. Böhm, U. Kuhl, N. Moiseyev, and S. Rotter, Encircling exceptional points as a non-Hermitian extension of rapid adiabatic passage, Phys. Rev. A **102**, 040201(R) (2020).
[8] I. I. Arkhipov, P. Lewalle, F. Nori, Ş. K. Özdemir, and K. B. Whaley, Topological state permutations in time-modulated non-Hermitian multiqubit systems with suppressed nonadiabatic transitions, Phys. Rev. Res. **7**, 033242 (2025).

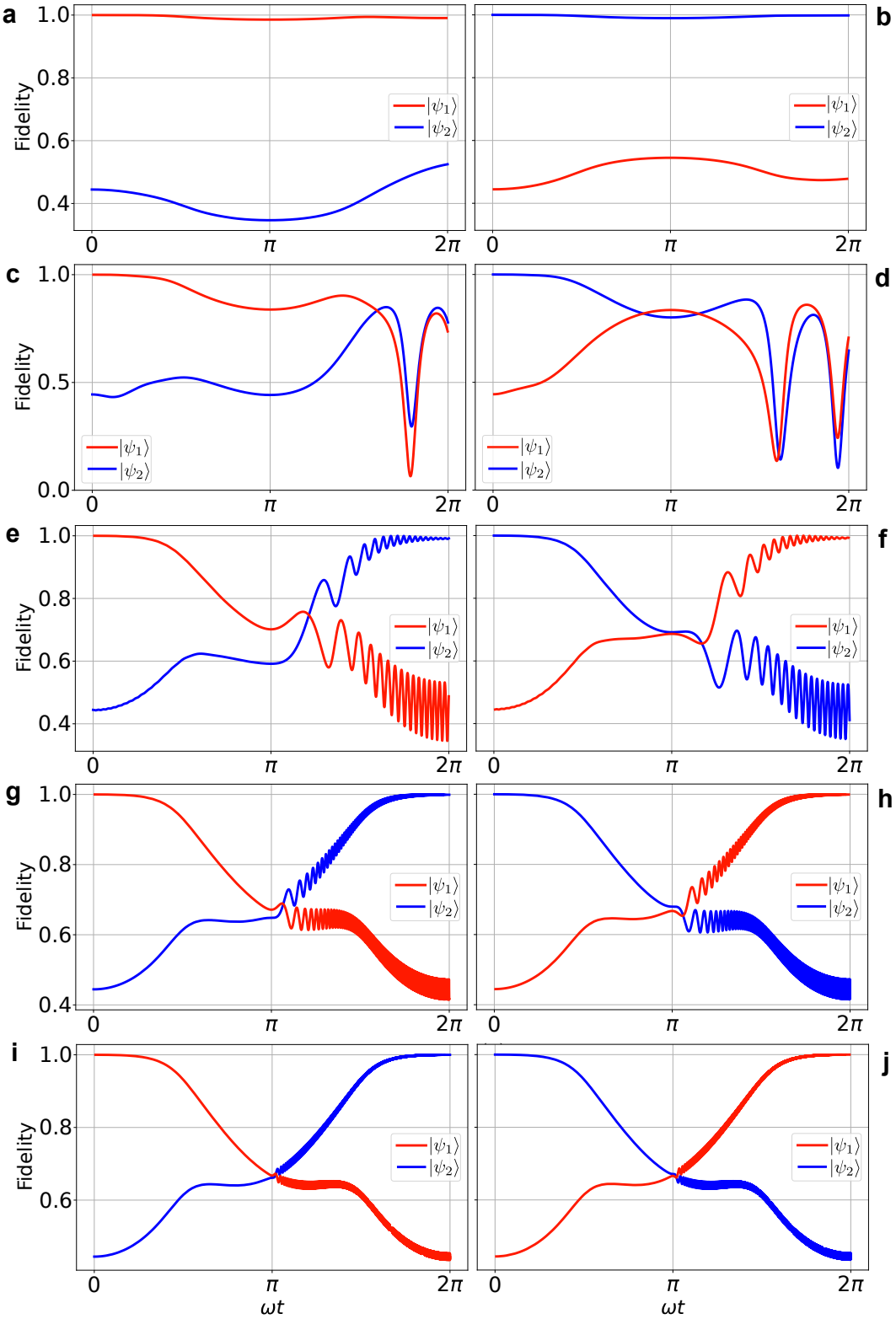

Supplementary Fig. 13. Similar to Fig. S3, but obtained from numerical simulations, showing the fidelity between the evolving and initial states for different values of the winding period T, irrespective of the winding direction. The left column corresponds to the case in which the initial state is chosen as $|\psi_1\rangle$, while the right column corresponds to $|\psi_2\rangle$. Each row corresponds to the EP-encircling protocol for the given period T, Namely, **a-b** $T = 1$ [arb. units], **c-d** $T = 10$ [arb. units], **e-f** $T = 100$ [arb. units], **g-h** $T = 1000$ [arb. units], **i-j** $T = 10000$ [arb. units]. The chosen loop trajectory around the EP is defined by the equations: $x = 0.2\sin(\omega t + \pi)$, and $y = 1 - 0.5\cos(\omega t + \pi)$. For this specific figure, the numerical simulations were performed using the Runge–Kutta method. The rapid oscillations observed in the second half of the winding period originate from the numerical stiffness encountered when crossing the diabolic line (further technical details regarding this solution stiffness can be found in Ref. [8], see Appendix G therein).

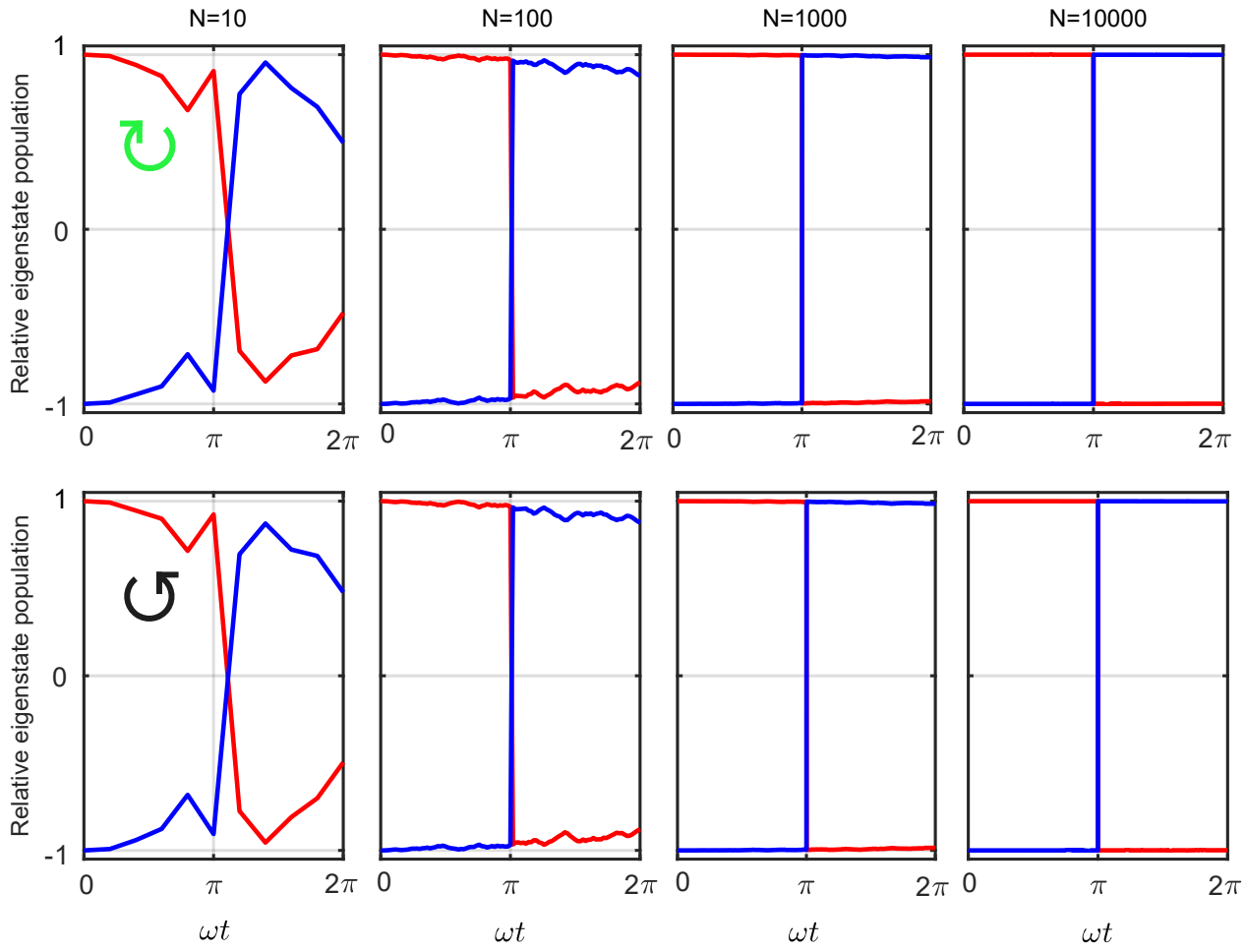

Supplementary Fig. 14. Convergence and robustness analysis of the adiabatic protocol for the discretization steps N. Numerical simulations of the relative eigenstate population $P(t)$ as a function of the discretization steps N and evolution speed ω for different N values ranging from 10 to 10^4 at a fixed speed $\omega = \pi/50000$. The red curves represent the evolution starting from the initial state $|\psi_1\rangle$, while the blue curves show the evolution from $|\psi_2\rangle$. The top row displays the results for clockwise (CW) encirclement, and the bottom row shows the results for counter-clockwise (CCW) encirclement. The results show that $P(t)$ converges rapidly to unity as N increases, with fluctuations becoming negligible for $N \geq 1000$. Other parameters are the same as those used in Fig. 2.

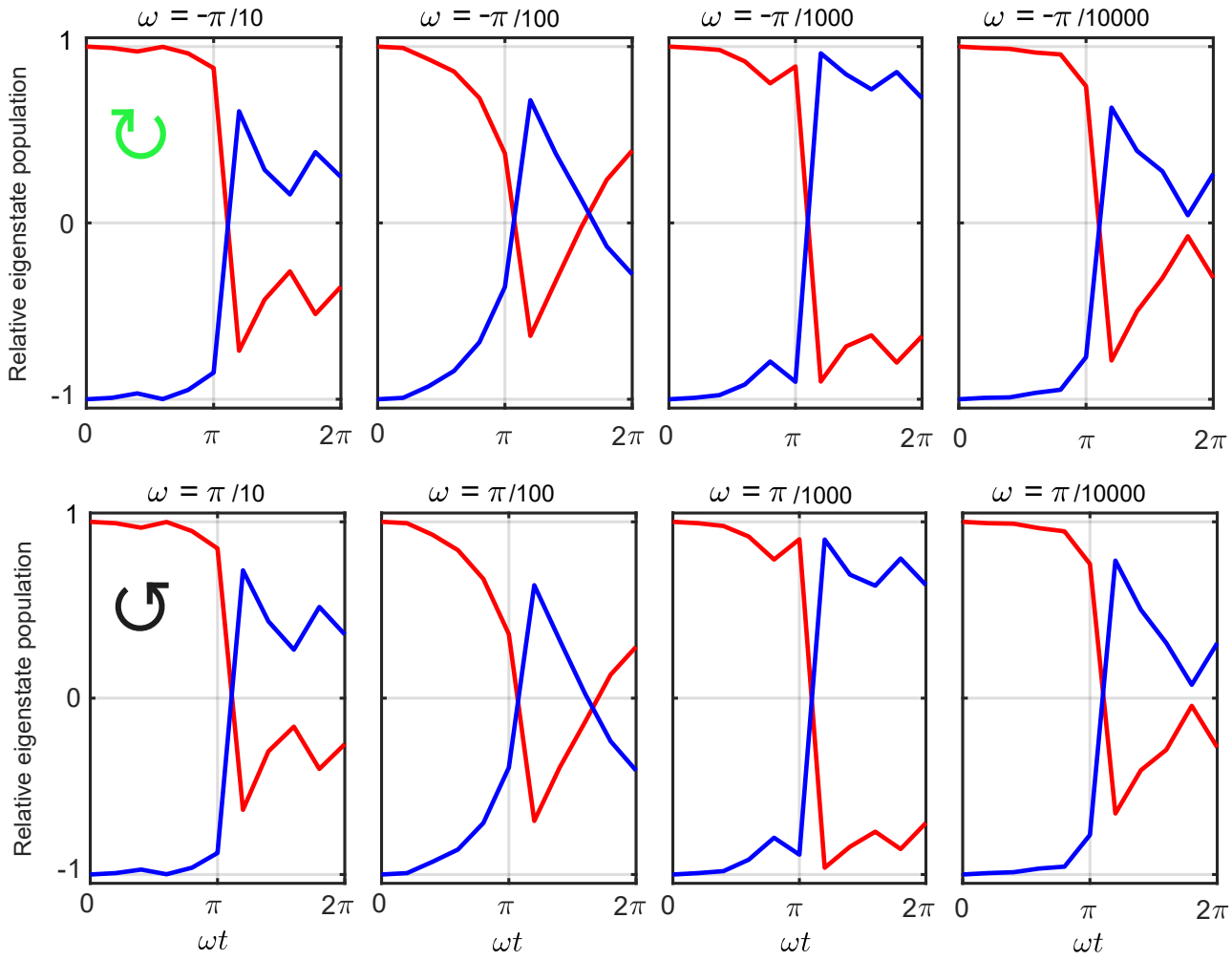

Supplementary Fig. 15. Numerical simulations of the relative eigenstate population $P(t)$ for various evolution speed ω and $N = 10$.

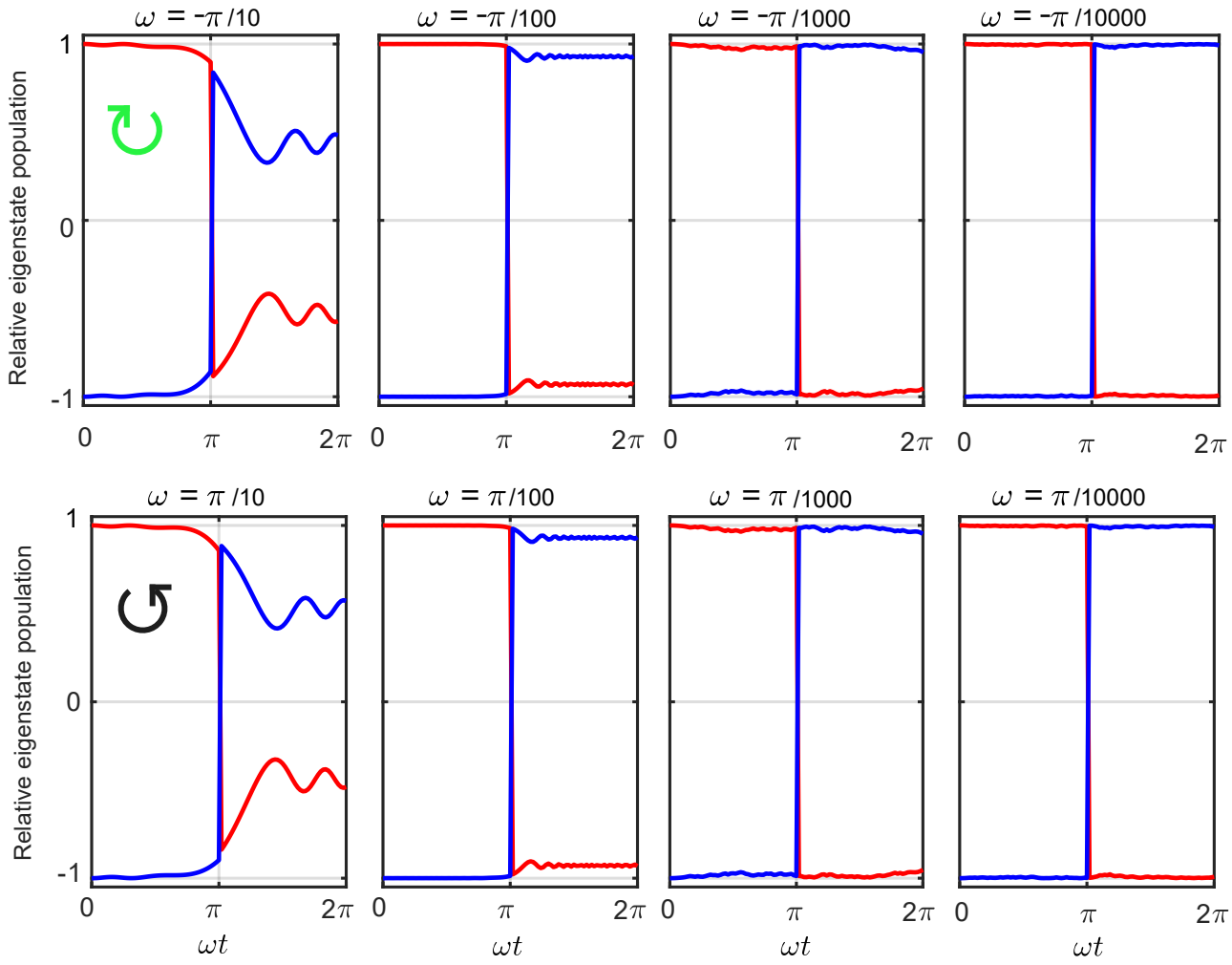

Supplementary Fig. 16. Numerical simulations of the relative eigenstate population $P(t)$ for various evolution speed ω and $N = 100$.

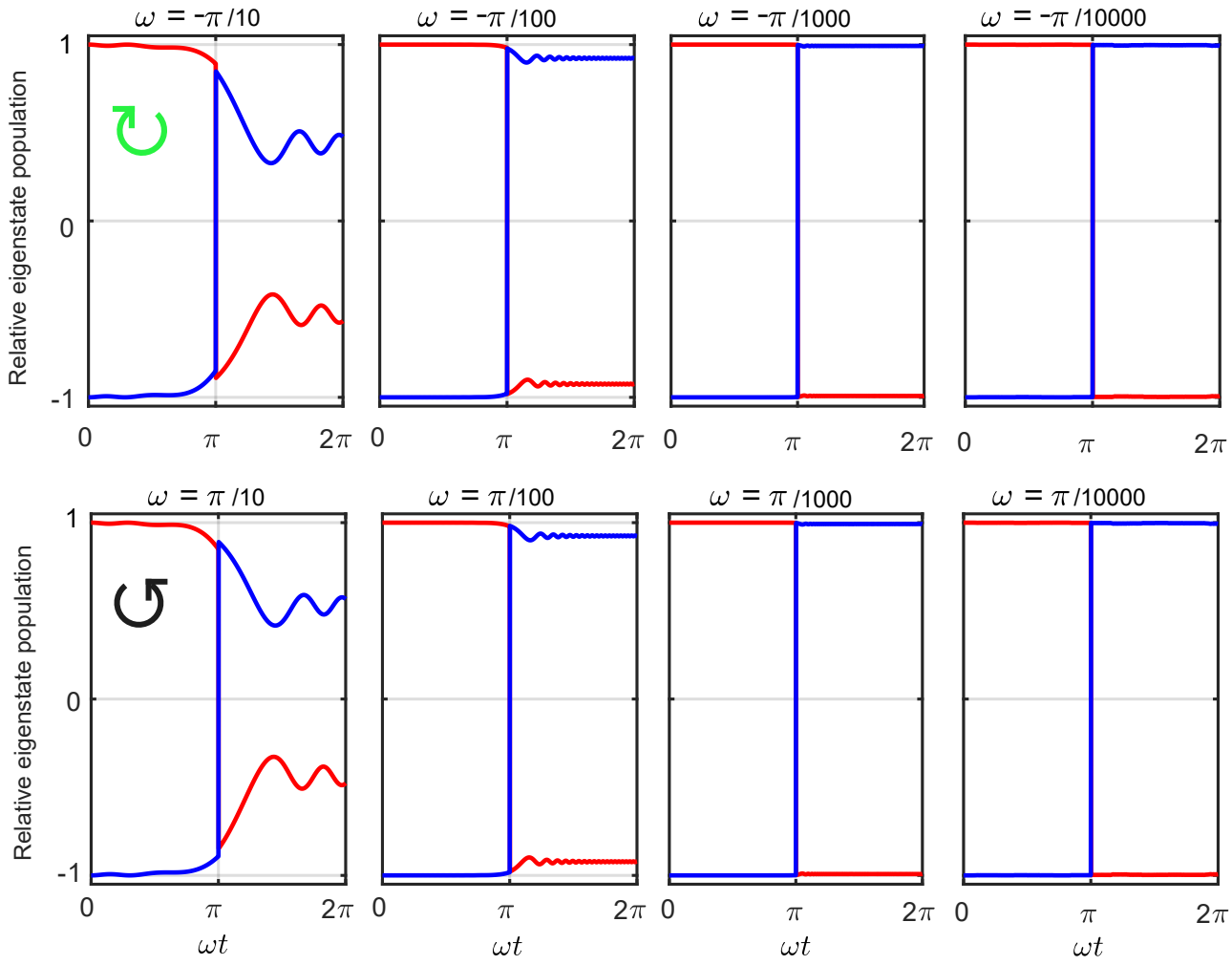

Supplementary Fig. 17. Numerical simulations of the relative eigenstate population $P(t)$ for various evolution speed ω and $N = 1000$.

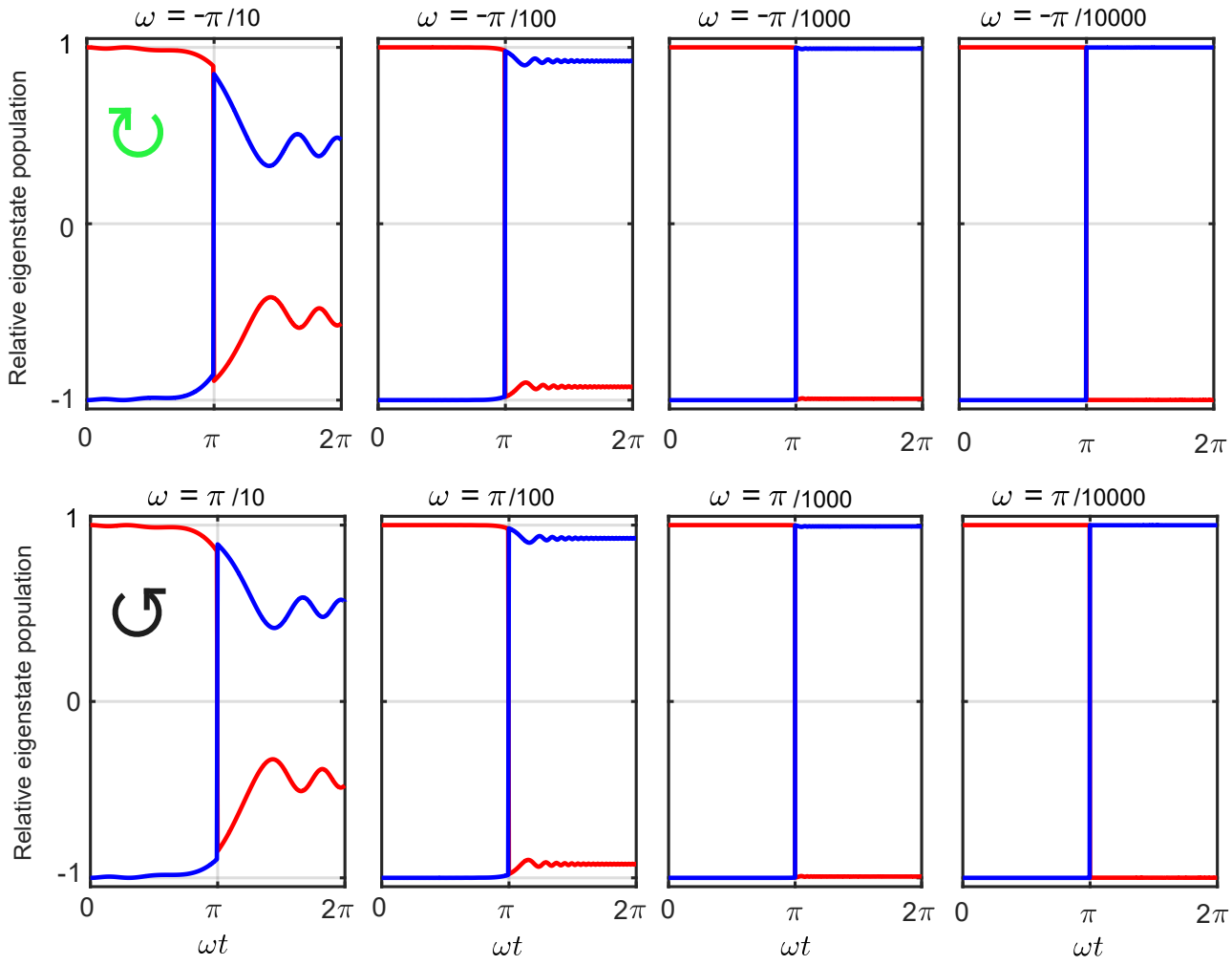

Supplementary Fig. 18. Numerical simulations of the relative eigenstate population $P(t)$ for various evolution speed ω and $N = 50000$.

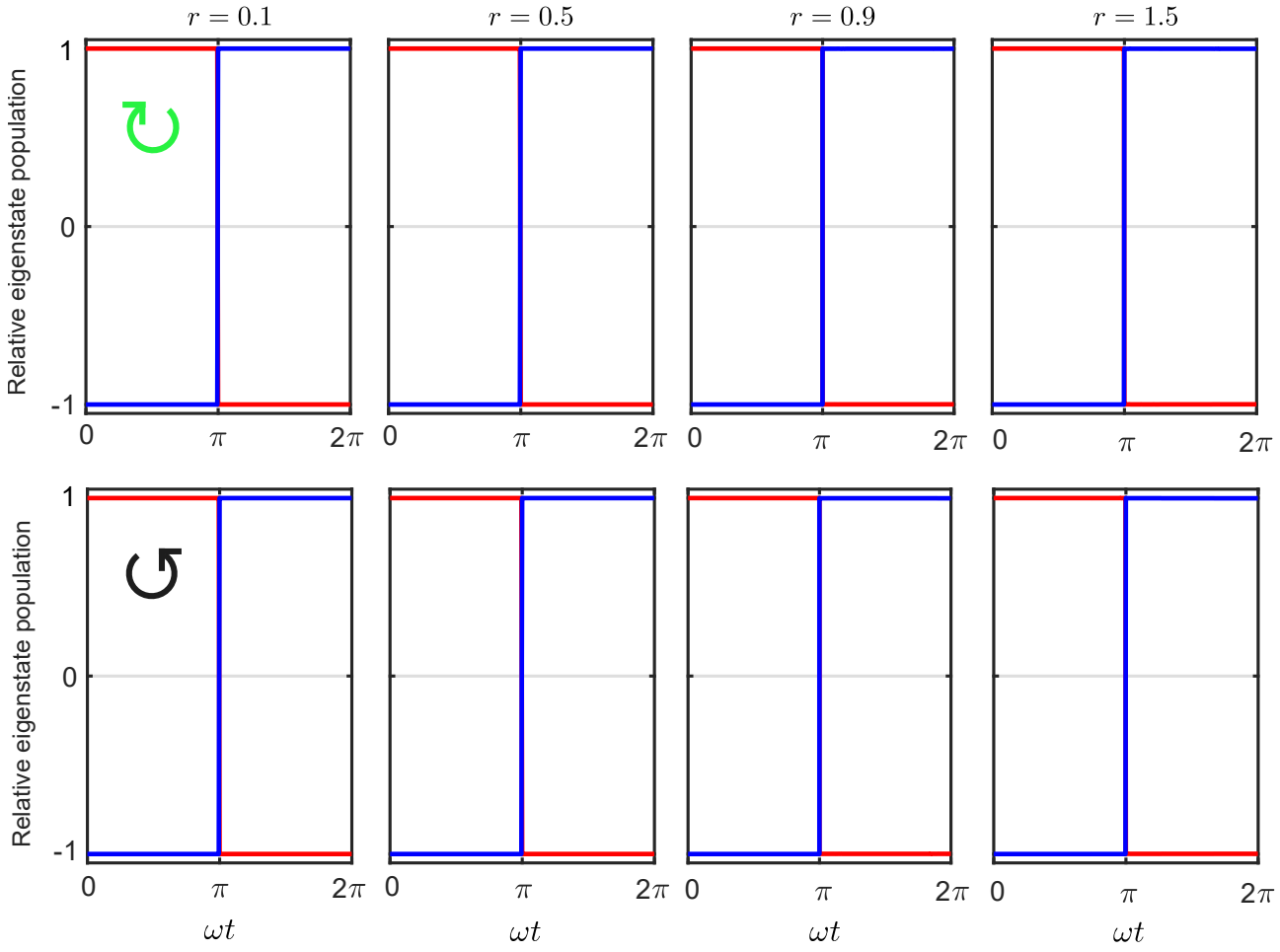

Supplementary Fig. 19. Numerical simulations of the relative eigenstate population $P(t)$ for various encirclement radius r around the EP, with $N = 50000$ and $w = \pi/50000$. The top row displays the results for CW, and the bottom row for CCW.

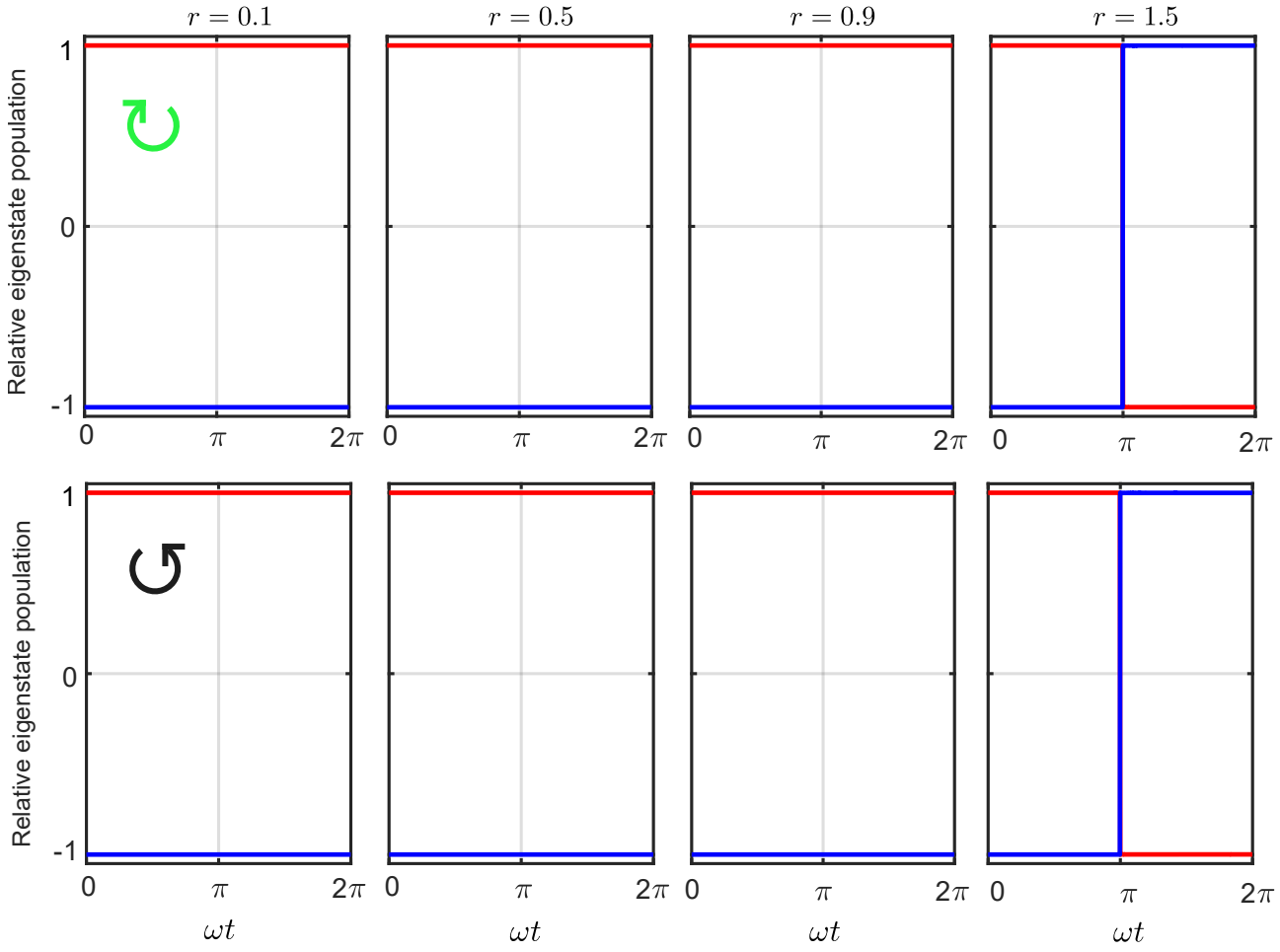

Supplementary Fig. 20. Numerical simulations of the relative eigenstate population $P(t)$ for the encirclement center is at (0,2), with $N = 50000$ and $w = \pi/50000$. The top row displays the results for CW, and the bottom row for CCW.